Applied Surface Science Advances 36 (2026) 101090

Contents lists available at ScienceDirect

Applied Surface Science Advances

journal homepage: www.sciencedirect.com/journal/applied-surface-science-advances

Full Length Article

Nanostructured titania–silica sol–gel multilayer coatings with spectrally selective light transmission and water-repellent functionality

Kinga Kovács [a], János Madarász [b], Norbert Nagy [c], Dániel Zámbó [c], Zoltán Hórvölgyi [a,*], Emőke Albert [a,*]

[a] Department of Physical Chemistry and Materials Science, Faculty of Chemical Technology and Biotechnology, Budapest University of Technology and Economics, Műegyetem rkp. 3., H-1111, Budapest, Hungary
[b] Department of Inorganic and Analytical Chemistry, Faculty of Chemical Technology and Biotechnology, Budapest University of Technology and Economics, Műegyetem rkp. 3., H-1111, Budapest, Hungary
[c] Institute of Technical Physics and Materials Science, HUN-REN Centre for Energy Research, Konkoly-Thege Miklós út 29-33, H-1121, Budapest, Hungary

ARTICLE INFO

Keywords:
Selective light transmittance
Water repellent property
Sol-gel coating
Thin-film systems
Glass substrate
Photovoltaic application

ABSTRACT

Spectrally selective multilayer titania–silica coatings with water-repellent functionality were developed on glass substrates by combining thin-layer optical modelling with sol–gel processing. A two-layer optical model was used to define suitable ranges of layer thickness and effective refractive index, which served as a basis for the experimental development and optimization of three- and four-layer coatings. The optimized glass/TiO_2/porous SiO_2/hybrid SiO_2 and glass/TiO_2/compact SiO_2/porous SiO_2/hybrid SiO_2 systems increased the average transmittance in the 400–700 nm range by 2.3 ± 0.4% and 2.3 ± 0.2%, respectively, while reducing the average near-infrared transmittance by 9.4 ± 0.6% and 7.8 ± 0.2%. Maximum transmittance values of 99.17 ± 0.11% at 498 ± 4 nm and 99.62 ± 0.07% at 554 ± 5 nm were achieved for the respective systems. The hybrid silica top layer enhanced visible-light transmission and provided water-repellent functionality, as demonstrated by low contact angle hysteresis and efficient droplet removal under a water jet. The coatings also showed sub-nanometer surface roughness and good optical stability under dry-heat exposure and water immersion, whereas abrasion caused visible surface scratches and a moderate increase in the root mean square error values. The results demonstrate that the combination of optical modelling and sol–gel processing provides an effective route to multilayer titania–silica coatings combining tailored spectral transmission with water-repellent surface functionality, offering a promising approach for functional photovoltaic cover-glass surfaces.

1. Introduction

The long-term performance of photovoltaic modules is affected by degradation under outdoor operating conditions, including light- and elevated-temperature-induced degradation [1–3]. This highlights the importance of advanced cover glass materials that can provide effective optical and environmental protection while maintaining high light transmission [4,5]. The efficiency and lifetime of photovoltaic modules are strongly influenced by environmental factors, including humidity, temperature fluctuations, ultraviolet exposure, wind, and surface contamination [6,7]. This challenge is particularly relevant for emerging technologies, such as perovskite solar cells, where environmental instability remains a major limitation [7]. Transparent glass covers provide an effective barrier against external degradation processes [7]; however, their functionality must also be optimized to ensure efficient light utilization by the photovoltaic device. Therefore, functional modifications of photovoltaic cover glass have attracted increasing attention as a promising approach to improve device performance [4,8–10] and durability [4,8,9].

The spectral distribution of incident solar radiation plays a critical role in photovoltaic performance and long-term stability [11]. For typical single junction perovskite solar cells with band gaps of approximately ~1.50–1.60 eV [12,13], the photoactive spectral range extends from the visible region toward wavelengths of approximately 800 nm [12–15]. The 400–700 nm interval represents the visible spectral range and encompasses a substantial portion of the spectral region in which perovskite photovoltaic devices exhibit strong photoresponse [12–15]. In typical perovskite solar cells, the external quantum efficiency (EQE)

* Corresponding authors.
E-mail addresses: horvolgyi.zoltan@vbk.bme.hu (Z. Hórvölgyi), albert.emoke@vbk.bme.hu (E. Albert).

https://doi.org/10.1016/j.apsadv.2026.101090
Received 10 August 2026; Received in revised form 5 October 2026; Accepted 22 October 2026
Available online 30 October 2026
2666-5239/© 2026 The Authors. Published by Elsevier B.V. This is an open access article under the CC BY-NC-ND license (http://creativecommons.org/licenses/by-nc-nd/4.0/).

generally remains close to its maximum throughout the visible range and typically extends at high levels to approximately 750 nm, before progressively decreasing toward the long-wavelength absorption edge [12–15]. For this reason, the 400–700 nm range was selected as it covers the central high-EQE region of perovskite solar cells while minimizing losses associated with attenuating the longer-wavelength photoactive region [15]. While photons with energies exceeding the active layer bandgap energy contribute to charge generation [10,11,16], the spectral response decreases toward the long-wavelength absorption edge. Ultraviolet radiation, in contrast, can accelerate degradation processes in perovskite solar cells through photoinduced chemical reactions, defect formation, and instability of functional layers [17–20]. Near-infrared (NIR) radiation below the absorber bandgap [12–14] contributes minimally to photocurrent generation [12,13,15,20] but increases parasitic heating, resulting in elevated operating temperatures and accelerated thermal degradation [21–24]. Therefore, optical management of the transmitted solar spectrum beyond the principal photoactive range can reduce unnecessary solar heating while maintaining adequate transmission within the useful spectral range. Spectrally selective light transmittance through photovoltaic cover materials thus represents an important approach for balancing efficient photon utilization, thermal management, and long-term device stability [25].

The development of photovoltaic cover glass coatings requires the optimization of multiple functional properties. Spectrally selective light transmittance [26,27], providing high transmission in the visible range while controlling unwanted spectral components, is essential for maximizing photon utilization and reducing parasitic heating. Water-repellent surface characteristics may facilitate water removal from the surface and thereby help reduce the retention of surface contaminants, potentially contributing to self-cleaning [8]. Achieving an appropriate combination of optimized optical performance and water-repellent surface properties remains a significant challenge in the development of advanced photovoltaic cover glass coatings [8,9].

Among available deposition techniques, the sol–gel process [28] is particularly attractive due to its low material consumption, cost-effectiveness, scalability, and versatile control over coating composition, structure, and thickness [4,29,30]. Thin-film coatings have been widely investigated for tailoring the optical and functional properties of surfaces through controlled modification of their composition, thickness, and structure [31–35]. Furthermore, optical modelling enables the rational optimization of multilayer structures by tailoring refractive index values and layer thicknesses to achieve the desired spectral response.

In this work, titania- and silica-based multilayer coatings were developed using a model-guided experimental approach that combines thin layer optical modelling [36,37] with the experimental development of more complex coating structures. The theoretical modelling was deliberately restricted to a two-layer system and was used to identify suitable combinations of refractive index and layer thickness as a starting point for achieving the targeted spectral behaviour. Direct extension of the model to the full four-layer structure would introduce additional coupled parameters and uncertainties associated with individual layer thicknesses, effective refractive indices, interfaces, and deviations from the idealized homogeneous-layer assumptions, thereby increasing the complexity of model optimization and interpretation [26,38,39]. Therefore, the two-layer model was not intended to quantitatively reproduce or replace the optical response of the subsequently developed three- and four-layer coatings. Instead, these structures were developed experimentally from the optical parameters identified by the two-layer model and further optimized based on their measured optical performance.

2. Experimental

2.1. Materials

Materials used for the synthesis of precursor sols: titanium(IV) butoxide (purum, ≥ 97%, Sigma-Aldrich), ethanol (EtOH, g.r., > 99.8%, Lach-Ner), nitric acid (special grade, 65%, Lach-Ner), tetraethoxysilane (TEOS, >99%, Acros Organics), methyl triethoxysilane (MTES, >99%, Sigma-Aldrich), 2-propanol (a.r. > 99.7%, Reanal, Hungary), hydrochloric acid (>36.5%, purum p.a., Fluka), cetyltrimethylammonium bromide (CTAB, >99%, Acros Organics), Pluronic P123 (P123, average $M_n \sim 5\,800$, Sigma-Aldrich), and ultrapure water (18.2 MΩ cm, purified with an Adrona Integrity+ filtration system).

Microscope glass slides (76 × 26 × 1 mm, Microscope Slides Epredia) and silicon wafers (Siegert, (100), p-type, prime grade) were used as solid substrates for the coatings. Substrates were cleaned with 2-propanol and ultrapure water. Prior to layer deposition, the cleaned silicon substrates underwent a 10-min O_2 plasma treatment (radiofrequency-generated low-pressure plasma/SmartPlasma 10, Plasma Technology GmbH, coupled with an oxygen concentrator/DeVilbiss Healthcare 525 KS) to improve their adhesion and wettability with the ethanolic precursor sol.

2-Propanol was used as the adsorptive material during the ellipsometric porosimetry measurements.

All materials were of analytical grade and were used without further purification.

2.2. Synthesis of precursor sols

The precursor sols for titania (TiO_2) coatings were prepared by the acid-catalysed controlled hydrolysis of titanium(IV) butoxide in ethanolic media. Nitric acid was used as a catalyst in the synthesis of precursor sol. The molar ratios for titanium(IV) butoxide:EtOH:HNO_3:H_2O were 1:27.95:0.49:0.82. The mixture was stirred for 2 h at 60 °C at 400 rpm [40,41].

The precursor sols for compact silica ($cSiO_2$) coatings were prepared by acid-catalysed controlled hydrolysis and polycondensation of tetraethyl orthosilicate in ethanolic medium. 0.1 M aqueous solution of hydrochloric acid was used as the catalyst. The molar ratios for TEOS:EtOH:HCl:H_2O were 1:4.68:7 × 10^{-3}:3.96, and the mixture was stirred at 25 °C for 1 h [33,42].

The precursor sols for porous silica ($pSiO_2$) coatings were prepared using Pluronic P123 as a structure-directing template. First, 2 g of the Pluronic P123 triblock copolymer was dissolved in 22 mL of ethanol. Separately, TEOS, ethanol, and 0.1 M HCl were mixed using the same molar ratios as those applied for the compact silica precursor sol, with a total solution volume of 35 mL. Both were stirred separately for 30 min at room temperature, followed by a further 30 min of stirring after they were combined [43].

The precursor sols for hybrid silica ($hSiO_2$) coatings were prepared using two silica precursors, TEOS and MTES. First, TEOS was mixed with aqueous hydrochloric acid solution (0.06 M, pH = 1.3) and ethanol, then the mixture was stirred for 1 h at 60.0 °C. The molar ratio for TEOS:H_2O:EtOH was 1:10:7.7. In another beaker, CTAB was dissolved in the mixture of ethanol and MTES and stirred for 30 min at room temperature. The molar ratio of MTES:CTAB:EtOH was 1:0.2:1. After the stirring, the two mixtures were poured together and stirred for further 15 min (400 rpm) at room temperature [34,44].

2.3. Preparation of the samples

Sol-gel coatings on solid substrates (glass, silicon) were prepared from the precursor sols by the dip-coating method at 25 °C by a dip-coater device (Plósz Mérnökiroda Kft., Hungary).

Cleaned and dried substrates were immersed in the precursor sols and withdrawn perpendicular to the liquid surface at constant

withdrawal speeds of 14; 15; 16; or 24 cm/min (TiO_2 precursor sol); 2 or 4 cm/min (compact SiO_2 precursor sol); 1; 3; or 5 cm/min (porous SiO_2 precursor sol); and 1; 2; 3; 4; 5; or 6 cm/min (hybrid SiO_2 precursor sol). Samples were heat treated in a drying oven (Nabertherm B170) at 450 °C for 30 min (TiO_2, compact SiO_2), 480 °C for 1 h (porous SiO_2), and 400 °C for 2 h (hybrid SiO_2). The heating rate was 5 °C/min for the TiO_2, 21 °C/min for the compact SiO_2, 23 °C/min for the porous SiO_2, and 13 °C/min for the hybrid SiO_2 coatings. The selected withdrawal speeds and heat-treatment conditions were based on previous experimental experience.

Powder TiO_2 sample for X-ray diffraction was prepared by drying out 1 ml of TiO_2 precursor sol in a ceramic holder, covered with perforated aluminium foil at room temperature, then heat treated with the same program as the TiO_2 coatings.

2.4. Characterization methods

2.4.1. Optical modelling of the sample coatings

Prior to the experimental work, thin-film optical modelling was performed to determine the target coating parameters and provide guidance for the development of multilayer structures. These models are applicable to symmetric systems, where identical films are formed on both sides of the substrate during the dip-coating process. Two models were utilized: a single-layer model (Film1–Substrate–Film1) and a two-layer model (Film2–Film1–Substrate–Film1–Film2). Developed by Erzsébet Hild, these models enable the calculation of theoretical optical spectra using a simple computational process [36,37].

2.4.2. UV–visible spectroscopy

Optical properties of coatings on glass substrates were measured by UV-visible spectroscopy. Transmittance spectra of the bare and coated glass substrates were taken using an Analytik Jena Specord 200–0318 UV–vis spectrophotometer in the wavelength range of 350–1100 nm with 1 nm resolution and a scanning speed of 10 nm/s. The obtained transmittance curves were analysed in terms of thin-film optical models. Transmittance spectra of the coatings were fitted with a homogeneous layer model, supposing perpendicular angle of incidence and identical homogeneous single-layers of the same material on both sides of the transparent substrate (Hild model) [36,37]. For the two-layered samples a two-layered optical model was applied. The fitting procedures provided effective refractive index (at 632.8 nm) and layer thickness values. The fitting procedure used a Levenberg – Marquardt algorithm. Total porosity of the TiO_2 and SiO_2 coatings was estimated, based on the obtained effective refractive index values, using the Lorentz-Lorenz formula, considering refractive index values of 2.400 and 1.462 for the bulk TiO_2 [45] and bulk SiO_2 [46], respectively [37].

The light transmission change of the samples compared to their bare glass substrates was characterized by the Average Transmittance Change (ATC). ATC was calculated from the difference of the integrated area of the transmittance spectra measured on the coated sample and the substrate in the wavelength range of 400 – 700 nm (visible wavelength range), and 701–1100 nm (NIR wavelength range) as presented by Eq. (1), where x and y denote the lower and upper limits of the evaluated wavelength range, respectively.

$$\mathrm{ATC} = \frac{\sum_{i=x}^{y}\left(T_{sampe} - T_{substrate}\right)}{y - x} \tag{1}$$

2.4.3. Spectroscopic ellipsometry (SE) and ellipsometric porosimetry (EP)

Optical properties of the single- and multilayered samples on silicon substrates were determined by spectroscopic ellipsometry (SE), using a Semilab's Sopra EP-12 ellipsometric porosimeter. The measurements were carried out at atmospheric pressure, at the angle of incidence of 60° in the wavelength range of 248.5 nm – 971.5 nm. The thickness and the effective refractive index (at 632.8 nm) of the coatings were determined by applying the Tauc-Lorentz (TiO_2) and Cauchy (SiO_2) dispersion models.

Ellipsometric porosimetry was used to determine the open porosity, pore size, and pore size distribution of the single-layered TiO_2 and SiO_2 coatings deposited on silicon substrates. The measurements were carried out by the same device (Semilab's Sopra EP-12). EP is a technique suitable for characterizing porous thin coatings for open porosity, surface area, pore size, and mechanical strength. EP is a coupled technique in which the vapour adsorption can be studied step-by-step through spectroscopic ellipsometry. During the measurement, vapour of the adsorptive material condenses in the pore system which induces effective refractive index shift. Measuring the adsorption and the desorption isotherms, the porosity of the sample can be determined, furthermore, the pore size distribution can be calculated based on the modified Kelvin equation in case of mesopores and the Dubinin–Radushkevich model for micropores. The TiO_2 and SiO_2 coatings were characterized by this method using 2-PrOH as adsorptive material. Before the measurement the samples were heated up to 175 °C for 15 min, then vacuumed. The 2-propanol adsorption-desorption isotherms were taken at 24 °C.

2.4.4. X-ray diffraction (XRD)

Crystallinity of the TiO_2 powder samples was characterized by X-ray diffractometer (Philips PANalytical X'pert Pro, with Cu-Kα radiation) and X'celerator detector. Measurements were carried out in the 2Θ = 4–84° range, with scanning rate of 20 s/step and step size of 0.0167°, applying the automatic divergence slit system with irradiated length of 15 mm.

2.4.5. Scanning electron microscopy (SEM)

Samples deposited onto silicon substrates, including $Si/TiO_2/pSiO_2/hSiO_2$ and $Si/TiO_2/cSiO_2/pSiO_2/hSiO_2$ multilayer structures, were characterized by a Zeiss LEO 1540-XB Field Emission Scanning Electron Microscope (FE-SEM) using an acceleration voltage of 5.00 kV. Both top-view and cross-sectional imaging modes were applied to investigate the surface morphology and cross-sectional structure of the coatings. The layer thickness values were determined from the cross-sectional SEM images.

2.4.6. Atomic force microscopy (AFM)

The surface morphology of the samples deposited on glass substrates was analyzed using an AIST–NT SmartSPM 1000 Atomic Force Microscope (AFM) operated in tapping mode. The acquired AFM data were processed using Gwyddion software [47].

2.4.7. Wettability measurements

Wettability properties of the samples were studied by the determination of advancing (Θ_A) and receding (Θ_R) water contact angles (CA). The contact angles were measured with a drop shape analyser (DSA30, KRÜSS GmbH) using the sessile drop method and the drop-build-up technique. Advancing contact angles were determined using a drop volume of 20 μL, and in the case of receding angles, a diminished volume of 10 μL (removing 10 μL from the 20 μL drop) was used. Measurements were performed in a closed chamber with a relative humidity greater than 95% on three parallel samples at 25.0 °C. The wetting liquid was ultrapure water. Advancing and receding values of water contact angles were determined from three droplets on each sample. In order to characterize the water-repellent property of the coatings the contact angle hysteresis (H) was determined using the Eq. (2):

$$H = \Theta_A - \Theta_R \tag{2}$$

The equilibrium contact angle (Θ) was calculated according to Eq. (3) [48]:

$$\Theta = cos^{-1}\left(\frac{\cos\Theta_A + cos\Theta_R}{2}\right) \tag{3}$$

2.4.8. Stability and durability tests

The stability and durability tests were performed according to the test categories and severity levels specified in ISO 9022–2:2015 [49] and ISO 9211–4:2012 [50]. Category C was selected for coatings on glass intended for outdoor applications with limited abrasion resistance. Accordingly, the coatings were subjected to dry-heat, abrasion, adhesion, and solubility tests. The abrasion resistance and adhesion of the coatings were evaluated using a Coating Hardness Kit (Summers Optical, a division of EMS Acquisition Corp.).

Thermal stability was tested by exposing the samples to a dry heat atmosphere at 70 ± 2 °C with a relative humidity below 40% for 6 h. Mechanical durability was assessed via a cheesecloth abrasion test, in which a cheesecloth pad was moved across the sample surface for 100 strokes at a frequency of approximately 1 stroke/s under an applied load of 5 ± 1 N. Coating adhesion was tested by applying a ~25 mm wide piece of pressure-sensitive adhesive tape onto the sample surface, smoothing it down firmly by hand to ensure complete contact, and quickly (1 s/25 mm of tape) peeling it off perpendicularly to the sample's surface. Water resistance was evaluated by fully immersing the samples in ultrapure water at 23 ± 2 °C for 6 h.

Following each test, the transmittance spectra of the samples were recorded over the 350–1100 nm wavelength range and compared with the corresponding spectra obtained before the treatment. The optical changes induced by the tests were quantified by calculating the root mean square error (RMSE) between the transmittance spectra measured before and after each treatment.

3. Results and discussion

The experimental results presented and discussed in this section are restricted to the coating systems that demonstrated the most favourable optical performance among the investigated deposition conditions and whose optical properties showed the best agreement with the predictions obtained from thin-film optical modelling. For these systems, the TiO_2 coating was deposited by two successive dip-coating cycles at a withdrawal speed of 14 cm/min, with a 30 min interval between the cycles, while the $cSiO_2$, $pSiO_2$, and $hSiO_2$ layers were deposited at withdrawal speeds of 2, 1, and 3 cm/min, respectively.

3.1. Thin-film optical modelling for coating parameter optimization

The objective of the optical modelling was to propose a coating system that enhances the transmittance in the visible light range while decreasing it in the near-infrared (NIR) range relative to the bare glass substrate. Among the applied optical models, the two-layer model provided the solution identified through systematic manual parameter optimization. This solution consisted of a two-layer structure: a 120–130 nm thick layer with a refractive index of n = 2 deposited on the glass substrate, followed by a 100 nm thick layer with a refractive index of n = 1.3 (Fig. 1).

Fig. 2 illustrates the optical response predicted by the thin-film optical model for the layer structure defined by the thickness and refractive index values obtained from optical modelling, together with the calculated ATC values for the visible (Vis: 400–700 nm) and near-infrared (NIR: 701–1100 nm) spectral ranges. These results provide an optical starting point for the target spectral characteristics used in the subsequent experimental development and evaluation of the multilayer coating systems.

Although optical modelling can, in principle, be extended to more complex multilayer configurations, increasing the number of layers introduces additional coupled parameters and uncertainties associated with layer thicknesses, effective refractive indices, interfaces, and deviations from the idealized homogeneous-layer assumptions. Such additional degrees of freedom complicate both model optimization and the direct interpretation of differences between calculated and experimental spectra. Therefore, the two-layer structure was deliberately used

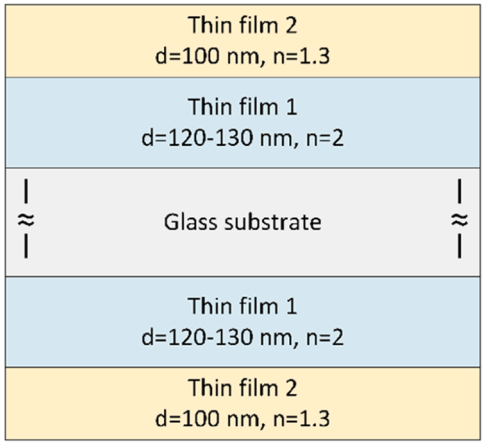


Fig. 1. Layer structure determined from UV–Vis spectral modelling using manual parameter adjustment (d: layer thickness; n: refractive index at 632.8 nm).

to establish an optical starting point for the subsequent experimental development of the more complex multilayer coatings.

Thin-film systems were subsequently prepared based on the modelling results, and further improvements in optical performance were explored experimentally through the preparation of three- and four-layer coating structures. Among the prepared samples, the systems showing the most favourable combination of spectral characteristics, selective optical transmittance, and water-repellent surface functionality were further characterized. The same preparation procedure was applied to silicon substrates to prepare corresponding thin-film samples for structural characterization.

3.2. Optical characterization of the developed coating samples

3.2.1. Light transmittance of the samples on glass substrates

Fig. 3 shows the representative, experimentally obtained transmittance spectra of the glass substrate and glass/TiO_2/$pSiO_2$/$hSiO_2$ (Fig. 3(a)) and glass/TiO_2/$cSiO_2$/$pSiO_2$/$hSiO_2$ (Fig. 3(b)) samples at different preparation stages: single-layer (glass/TiO_2 Fig. 3(a) and (b)), two-layer (glass/TiO_2/$pSiO_2$ Fig. 3(a), glass/TiO_2/$cSiO_2$ Fig. 3(b)), three-layer (glass/TiO_2/$pSiO_2$/$hSiO_2$ Fig. 3(a), glass/TiO_2/$cSiO_2$/$pSiO_2$ Fig. 3(b)), and four-layer (glass/TiO_2/$cSiO_2$/$pSiO_2$/$hSiO_2$ Fig. 3(b)) samples. Across the investigated multilayer structures, increasing the number of layers generally increased the visible-light transmission, while the introduction of additional silica-based layers modified the spectral distribution through interference-driven modulation of near-infrared transmittance.

Optical evaluation was limited to single- and two-layer thin-film models; thus, only the optical properties (thickness, effective refractive index, and estimated total porosity) of the TiO_2 and $pSiO_2$ (for the glass/TiO_2/$pSiO_2$/$hSiO_2$ type sample, Fig. 3(a)), as well as the TiO_2 and $cSiO_2$ (for the glass/TiO_2/$cSiO_2$/$pSiO_2$/$hSiO_2$ type sample, Fig. 3(b)) layers could be determined from spectra recorded after annealing. Four samples of both coating types were analyzed. The optical properties of the coatings are summarized in Table 1, while the ATC values calculated from the transmittance spectra recorded after each coating deposition and subsequent heat treatment step for the glass/TiO_2/$pSiO_2$/$hSiO_2$ and glass/TiO_2/$cSiO_2$/$pSiO_2$/$hSiO_2$ samples are summarized in Table 2. The glass/TiO_2/$pSiO_2$/$hSiO_2$ and glass/TiO_2/$cSiO_2$/$pSiO_2$/$hSiO_2$ structures showed positive ATC values of 2.3 ± 0.4% and 2.3 ± 0.2% in the visible range, respectively, together with negative ATC values of −9.4 ± 0.6% and −7.8 ± 0.2% in the near-infrared range (Table 2). The transmittance maxima for the glass/TiO_2/$pSiO_2$/$hSiO_2$ and glass/TiO_2/$cSiO_2$/$pSiO_2$/$hSiO_2$ samples were 99.17 ± 0.11% and 99.62 ± 0.07% at wavelengths of 498 ± 4 nm and 554 ± 5 nm, respectively (Table 3). Consistent with

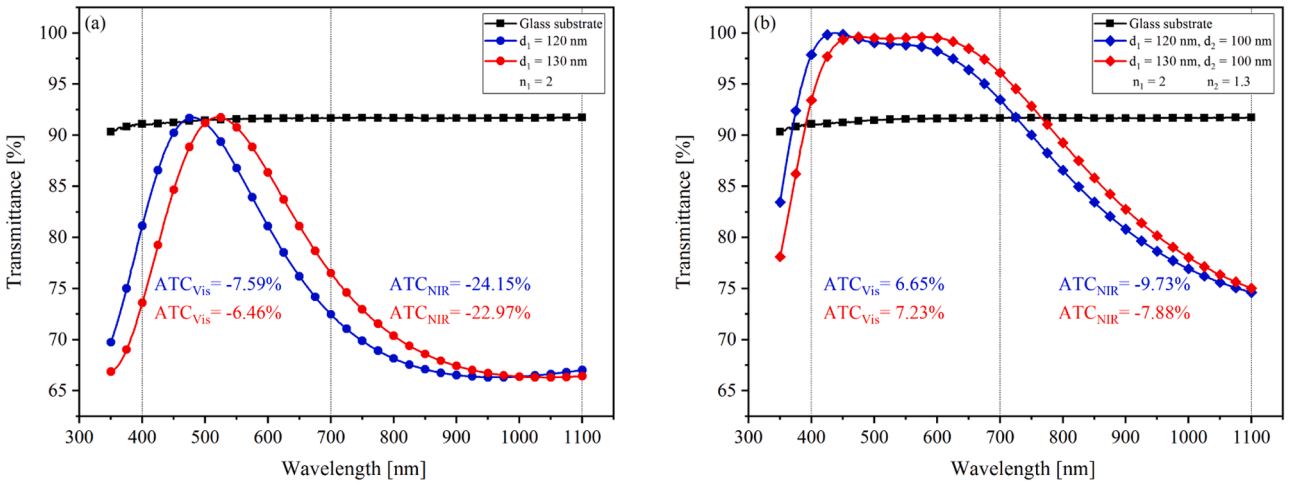


Fig. 2. Transmittance spectra calculated by thin-film optical modelling for (a) single-layer and (b) two-layer configurations, showing the corresponding layer thickness (d), refractive index (n), and Average Transmittance Change (ATC) values for the visible (Vis, 400–700 nm) and near-infrared (NIR, 701–1100 nm) wavelength ranges.

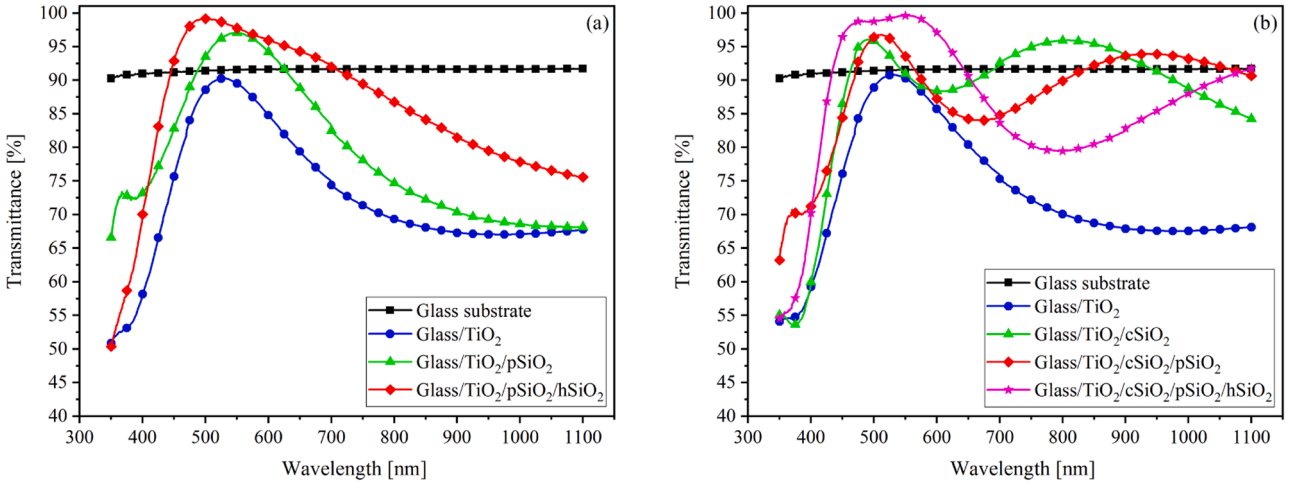


Fig. 3. Representative, experimentally obtained transmittance spectra of the glass substrate, (a) glass/TiO_2/$pSiO_2$/$hSiO_2$ and (b) glass/TiO_2/$cSiO_2$/$pSiO_2$/$hSiO_2$ samples at different preparation stages: single-layer (glass/TiO_2 (a) and (b)), two-layer (glass/TiO_2/$pSiO_2$ (a), glass/TiO_2/$cSiO_2$ (b)), three-layer (glass/TiO_2/$pSiO_2$/$hSiO_2$ (a), glass/TiO_2/$cSiO_2$/$pSiO_2$ (b)), and four-layer glass/TiO_2/$cSiO_2$/$pSiO_2$/$hSiO_2$ (b) samples.

Table 1
Optical properties of the coatings determined by UV–vis spectroscopy: thickness (d), effective refractive index at 632.8 nm (n), and total porosity calculated using the Lorentz–Lorenz equation. For the glass/TiO_2/$pSiO_2$/$hSiO_2$ samples, the properties of the TiO_2 and $pSiO_2$ layers are reported, whereas for the glass/TiO_2/$cSiO_2$/$pSiO_2$/$hSiO_2$ samples, those of the TiO_2 and $cSiO_2$ layers are reported. Values are presented as the mean ± sample standard deviation calculated from four independently prepared samples of the same coating type.

Sample	TiO_2			$pSiO_2$			$cSiO_2$		
	d [nm]	n [-]	Total p [%] Lorentz-Lorenz	d [nm]	n [-]	Total p [%] Lorentz-Lorenz	d [nm]	n [-]	Total p [%] Lorentz-Lorenz
glass/TiO_2/ $pSiO_2$/$hSiO_2$	124 ± 1	2.081 ± 0.005	14.2 ± 0.3	68 ± 4	1.195 ± 0.021	54.6 ± 4.7	-	-	-
glass/TiO_2/ $cSiO_2$/$pSiO_2$/$hSiO_2$	124 ± 1	2.085 ± 0.008	14.0 ± 0.4	-	-	-	131 ± 1	1.424 ± 0.007	7.2 ± 1.3

the transmittance spectra (Fig. 3), the $hSiO_2$-free structures (glass/TiO_2/$pSiO_2$ and glass/TiO_2/$cSiO_2$/$pSiO_2$) yielded negative ATC values in the visible range, indicating that the addition of the $hSiO_2$ layer contributed to the enhancement of visible-light transmittance (Table 2).

3.2.2. Thickness, effective refractive index, porosity and pore-size distribution of the samples by SE and EP

The optical properties of single- and multilayer samples deposited onto silicon substrates were characterized by spectroscopic ellipsometry (SE). Measurements were carried out at atmospheric pressure. The thickness and effective refractive index (at 632.8 nm) values were obtained using the Tauc–Lorentz and Cauchy dispersion models for the

Table 2
The average transmittance change (ATC) values of the glass/TiO_2/$pSiO_2$/$hSiO_2$ and glass/TiO_2/$cSiO_2$/$pSiO_2$/$hSiO_2$ samples, calculated from experimental transmittance spectra. Values calculated after each conditioning step (1/2/3) for the visible (Vis) and near-infrared (NIR) wavelength range are presented. Values corresponding to the final samples are shown in bold. Values are presented as the mean ± sample standard deviation calculated from four independently prepared samples of the same coating type.

Sample	ATC Vis-1	ATC Vis-2	ATC Vis-3	ATC Vis-4	ATC NIR-1	ATC NIR-2	ATC NIR-3	ATC NIR-4
glass/TiO_2/$pSiO_2$/$hSiO_2$	−10.3 ± 0.3	−2.1 ± 0.3	**2.3 ± 0.4**	-	−23.3 ± 0.4	−19.8 ± 0.4	**−9.4 ± 0.6**	-
glass/TiO_2/$cSiO_2$/$pSiO_2$/$hSiO_2$	−9.9 ± 0.2	−3.1 ± 0.3	−4.3 ± 0.4	**2.3 ± 0.2**	−22.8 ± 0.4	0.1 ± 0.3	−0.4 ± 0.0	**−7.8 ± 0.2**

Table 3
The maximum transmittance (T_{max}) and corresponding wavelength (λ) values of the glass/TiO_2/$pSiO_2$/$hSiO_2$ and glass/TiO_2/$cSiO_2$/$pSiO_2$/$hSiO_2$ samples, determined from experimental transmittance spectra. Values determined after each conditioning step (1/2/3) are presented. Values corresponding to the final samples are shown in bold. Values are presented as the mean ± sample standard deviation calculated from four independently prepared samples of the same coating type.

Sample	T_{max} [%] 1	T_{max} [%] 2	T_{max} [%] 3	T_{max} [%] 4	λ [nm] 1	λ [nm] 2	λ [nm] 3	λ [nm] 4
glass/TiO_2/$pSiO_2$/$hSiO_2$	90.60 ± 0.32	97.16 ± 0.19	**99.17 ± 0.11**	-	526 ± 5	545 ± 5	**498 ± 4**	-
glass/TiO_2/$cSiO_2$/$pSiO_2$/$hSiO_2$	90.86 ± 0.18	96.34 ± 0.20	96.67 ± 0.27	**99.62 ± 0.07**	530 ± 1	490 ± 1	510 ± 1	**554 ± 5**

TiO_2 and different SiO_2 layers, respectively. The results are summarized in Table 4.

The thickness and effective refractive index values obtained by spectroscopic ellipsometry for the TiO_2 coatings deposited on Si substrates show only minor variations among the investigated systems (Table 4). The TiO_2 coatings have thicknesses of 125–134 nm and effective refractive indices of 2.132–2.139, indicating relatively consistent layer thicknesses and effective refractive indices within the silicon-supported coating systems. Compared with the TiO_2 layers deposited on glass, which have thicknesses of 124 nm and effective refractive indices of 2.081–2.085 (Table 1), the layer thicknesses are similar, whereas the effective refractive indices determined on Si substrates are approximately 2–3% higher. Thus, the TiO_2 layer thicknesses are comparable for the two substrate systems, while a moderate difference is observed in the effective refractive index values.

In contrast, the SiO_2 coatings show more pronounced variations depending on the underlying substrate or coating. The $cSiO_2$ layer deposited directly onto the Si substrate has a thickness of 109 nm and an effective refractive index of 1.442, whereas its thickness increases to 120–124 nm and its effective refractive index decreases to 1.425–1.426 when deposited on TiO_2-containing coating systems. The $pSiO_2$ coating shows thicknesses of 44–66 nm and effective refractive indices of 1.185–1.270, depending on the substrate and underlying coating layers. In particular, the $pSiO_2$ layers deposited on TiO_2 have thicknesses of 44–48 nm, which are approximately 29–35% lower than the thickness of 68 ± 4 nm determined for the glass-supported system. Their effective refractive indices of 1.185–1.193, however, are close to the value of 1.195 ± 0.021 obtained for the glass-supported system. When deposited on the TiO_2/$cSiO_2$ bilayer, the $pSiO_2$ thickness increases to 60 nm, indicating that the $pSiO_2$ layer thickness is influenced by the combined effects of the substrate and the underlying coating layers.

A more pronounced variation is observed for the $hSiO_2$ coating. When deposited directly onto Si, the $hSiO_2$ layer has a thickness of 126 nm and an effective refractive index of 1.232, whereas in the multilayer systems its thickness decreases to 61–73 nm and its effective refractive index increases to 1.262–1.301.

It should be noted that the optical parameters of the glass- and silicon-supported samples were obtained using different approaches, namely transmittance-based optical modelling and spectroscopic ellipsometry, respectively. Therefore, the differences observed between the two substrate systems cannot be attributed exclusively to the substrate.

Overall, the results indicate that the TiO_2 layer thicknesses are relatively consistent among the investigated systems, while the effective refractive index values show a moderate difference between the glass- and silicon-supported samples. In contrast, the optical parameters of the SiO_2 coatings are influenced by the combined effects of the substrate and the underlying coating layers, with the magnitude of the variation depending on the coating type and layer configuration.

Single-layer TiO_2, $cSiO_2$, $pSiO_2$, and $hSiO_2$ samples deposited on silicon substrates were also analyzed by ellipsometric porosimetry (EP). Three samples of each coating type were analyzed. Adsorption and desorption isotherms were taken at 24 °C using isopropanol as adsorptive material. The adsorption-desorption isotherms, along with the normalized pore radius distribution functions determined by the modified Kelvin equation (for mesopores) and the Dubinin-Radushkevich model (for micropores), are presented in Fig. 4.

The ellipsometric porosimetry measurements revealed substantial differences in the pore structure of the investigated oxide coatings, reflecting the different synthesis strategies employed. The TiO_2 and $cSiO_2$ coatings were prepared from template-free sols, whereas the $pSiO_2$ and $hSiO_2$ coatings were synthesized using Pluronic P123 and

Table 4
Optical parameters of thin-film systems deposited on silicon substrates determined by spectroscopic ellipsometry (d: layer thickness, n: effective refractive index at 632.8 nm).

Sample	TiO_2		$cSiO_2$		$pSiO_2$		$hSiO_2$	
	d [nm]	n [-]	d [nm]	n [-]	d [nm]	n [-]	d [nm]	n [-]
Si/TiO_2	125	2.136	-	-	-	-	-	-
Si/$cSiO_2$	-	-	109	1.442	-	-	-	-
Si/$pSiO_2$	-	-	-	-	66	1.270		
Si/$hSiO_2$	-	-	-	-	-	-	126	1.232
Si/TiO_2/$cSiO_2$	130	2.139	124	1.426	-	-	-	-
Si/TiO_2/$pSiO_2$	127	2.132	-	-	44	1.185	-	-
Si/TiO_2/$cSiO_2$/$pSiO_2$	129	2.139	120	1.425	60	1.224	-	-
Si/TiO_2/$pSiO_2$/$hSiO_2$	134	2.132	-	-	48	1.193	61	1.262
Si/TiO_2/$cSiO_2$/$pSiO_2$/$hSiO_2$	130	2.139	120	1.425	60	1.222	73	1.301

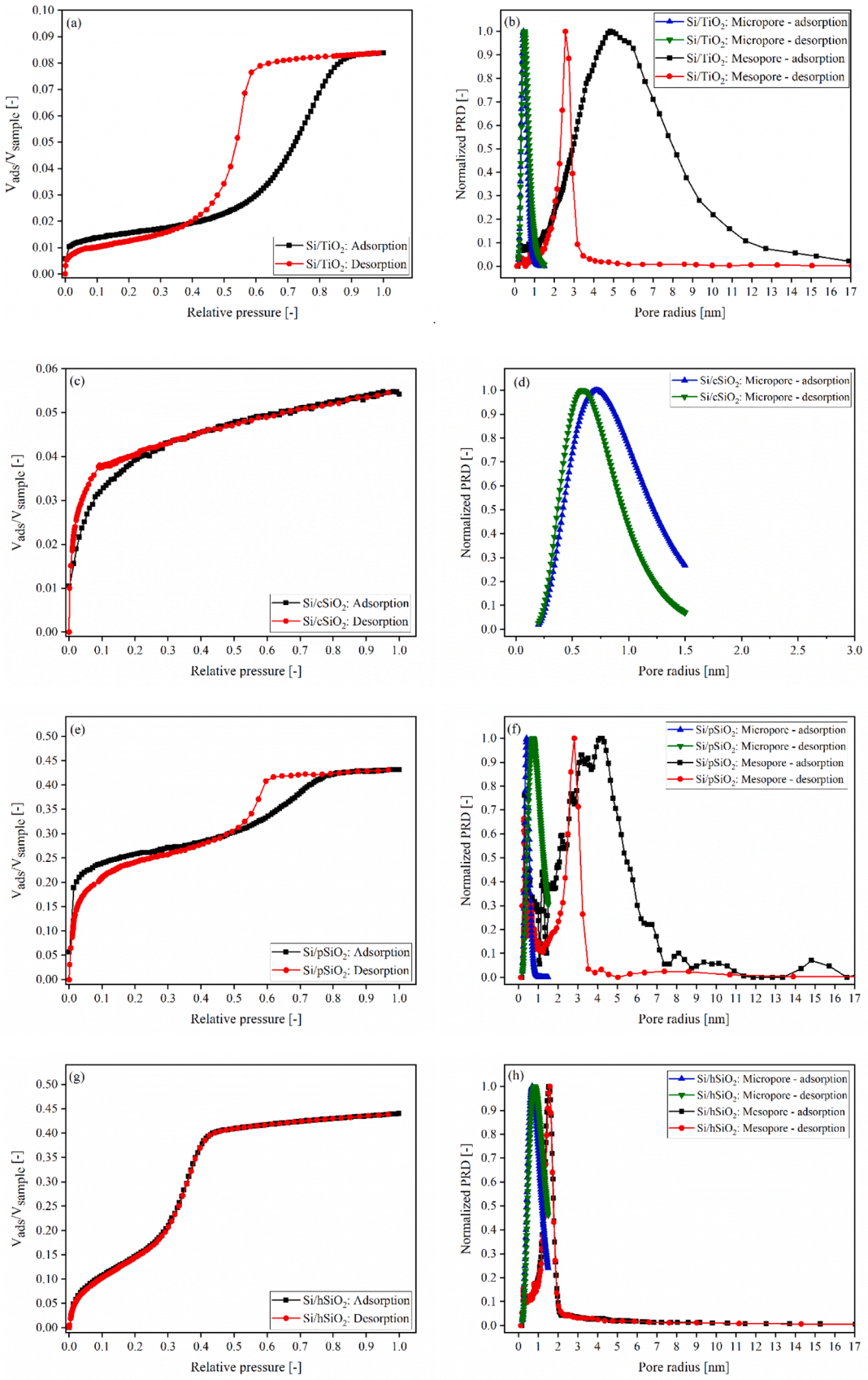


Fig. 4. Isopropanol adsorption-desorption isotherms (a, c, e, g) and normalized pore radius distribution functions (b, d, f, h) determined by ellipsometric porosimetry (EP) measured on single-layer TiO_2 (a, b), $cSiO_2$ (c, d), $pSiO_2$ (e, f), and $hSiO_2$ (g, h) coatings deposited on silicon substrates.

CTAB structure-directing agents, respectively. These differences are clearly reflected in the adsorption-desorption isotherms and the corresponding pore size distributions (Fig. 4).

The TiO_2 coating showed a pronounced hysteresis loop associated with capillary condensation at intermediate relative pressures ($p/p_o \sim 0.5–0.9$), indicating the presence of mesoporous structures. The adsorption–desorption isotherm showed a type IV isotherm according to the IUPAC classification, which is characteristic of mesoporous materials. The pore size distribution revealed a hierarchical micro-/mesoporous structure, with micropores characterized by radii of 0.45 ± 0.08 nm and 0.51 ± 0.01 nm and mesopores with characteristic pore radii of 5.30 ± 0.65 nm and 2.57 ± 0.01 nm determined from the adsorption and desorption branches, respectively. The relatively broad hysteresis loop suggests a heterogeneous mesoporous network with interconnected pore structures. The analysis confirmed an accessible open porosity of $8.32 \pm 0.13\%$ (Fig. 4 (a, b) and Table 5).

In contrast, the $cSiO_2$ coating showed a steep adsorbate uptake at very low relative pressures, followed by a gradual increase over the entire pressure range with only a weak hysteresis loop. The adsorption–desorption isotherm corresponds to a type I isotherm according to the IUPAC classification, characteristic of predominantly microporous materials. The pore size distribution confirmed the dominant microporous character of the coating, with characteristic pore radii 0.72 ± 0.03 nm and 0.59 ± 0.01 nm, while no significant mesopore contribution was observed. The weak hysteresis suggests minor structural heterogeneity or a limited contribution from larger pores. Consequently, the coating had the lowest accessible open porosity among the investigated samples ($5.72 \pm 0.04\%$). (Fig. 4 (c, d) and Table 5).

The $pSiO_2$ coating was characterized by a pronounced capillary condensation step in the intermediate relative pressure range, accompanied by a distinct hysteresis loop, indicating a type IV adsorption–desorption behaviour according to the IUPAC classification, characteristic of mesoporous materials. The significant adsorbate uptake at very low relative pressures additionally suggests the presence of micropores, indicating a hierarchical micro-/mesoporous pore structure of the coating. The development of this templated mesoporous network can be attributed to the use of the Pluronic P123 structure-directing agent during synthesis, which promotes the formation of mesopores through a self-assembly-driven templating mechanism. The pore size analysis revealed dominant mesopores with characteristic pore radii of 5.11 ± 1.74 nm and 3.11 ± 0.49 nm determined from the adsorption and desorption branches, respectively. The broad pore size distribution extending toward larger radii suggests a heterogeneous mesoporous network comprising mesopores with a range of sizes, while the observed hysteresis behaviour indicates interconnected pores with varying pore neck dimensions. The $pSiO_2$ coating showed a high accessible open porosity of $42.68 \pm 1.77\%$, consistent with its well-developed mesoporous network (Fig. 4 (e, f) and Table 5).

Among all samples, the $hSiO_2$ coating exhibited the most uniform pore structure. The adsorption and desorption branches nearly overlapped over the entire relative pressure range, indicating negligible hysteresis and highly reversible adsorption–desorption behaviour. Although the isotherm showed a capillary condensation step, the absence of a pronounced hysteresis loop suggests a relatively uniform mesoporous structure with limited pore-blocking effects. This behaviour is consistent with the pore size distribution, where adsorption- and desorption-derived analyses yielded similar characteristic mesopore radii of 1.62 ± 0.26 nm and 1.63 ± 0.35 nm, indicating a narrow pore size distribution. The coating was also characterized by the highest accessible open porosity of $44.64 \pm 2.79\%$ (Fig. 4 (g, h) and Table 5).

The open porosity values determined by EP (Table 4) are lower than the respective porosity values estimated from the effective refractive indices using the Lorentz–Lorenz equation (Table 1). This difference arises from the different types of porosity determined by the two methods. The Lorentz–Lorenz-derived values represent the total porosity, including both open and closed pores, whereas EP determines the open porosity accessible to the adsorbate molecules. The higher values obtained using the Lorentz–Lorenz equation are therefore consistent with the presence of a fraction of closed or otherwise inaccessible pores (see Tables 1 and 5).

3.3. Characterization of the TiO_2 sample by XRD

The TiO_2 powder sample was synthesized from the precursor sol used for TiO_2 layer deposition, and its XRD pattern is shown in Fig. 5. As anticipated from the annealing temperature applied during sample preparation, the diffraction peak can be assigned to the anatase crystalline phase of TiO_2 [PDF 00–021–1272] [51].

3.4. Characterization of the samples by field-emission scanning electron microscopy (FESEM)

The representative top-view and cross-sectional SEM images of the

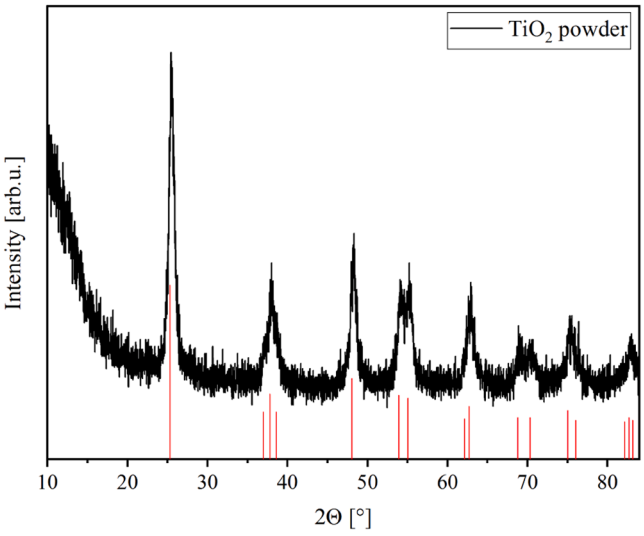


Fig. 5. XRD pattern of the TiO_2 powder sample. The standard diffraction peak positions of anatase [PDF 00–021–1272] are indicated by vertical bars at the bottom of the figure.

Table 5
EP analysis results for single-layer Si/TiO_2, Si/$cSiO_2$, Si/$pSiO_2$, and Si/$hSiO_2$ samples: open porosity and characteristic pore radius values in the micro- and mesopore ranges. Values are presented as the mean ± sample standard deviation calculated from three independently prepared samples of the same coating type.

Sample	Open p [%]	Pore radius [nm]			
		Micropores		Mesopores	
		adsorption	desorption	adsorption	desorption
Si/TiO_2	8.32 ± 0.13	0.45 ± 0.08	0.51 ± 0.01	5.30 ± 0.65	2.57 ± 0.01
Si/$cSiO_2$	5.72 ± 0.04	0.72 ± 0.03	0.59 ± 0.01	-	-
Si/$pSiO_2$	42.68 ± 1.77	0.47 ± 0.10	0.73 ± 0.04	5.11 ± 1.74	3.11 ± 0.49
Si/$hSiO_2$	44.64 ± 2.79	0.67 ± 0.19	0.64 ± 0.17	1.62 ± 0.26	1.63 ± 0.35

$Si/TiO_2/pSiO_2/hSiO_2$ and $Si/TiO_2/cSiO_2/pSiO_2/hSiO_2$ samples are presented in Fig. 6. Top-view SEM images (Fig. 6 (a, b)) revealed a homogeneous morphology of the samples. The layer thickness values determined from the cross-sectional images (Fig. 6 (c, d)) are summarized in Table 6. The TiO_2 layer is clearly distinguishable from the other layers, with thickness values of 116 ± 3 nm and 103 ± 4 nm for the $Si/TiO_2/pSiO_2/hSiO_2$ and $Si/TiO_2/cSiO_2/pSiO_2/hSiO_2$ samples, respectively. The compact silica layer ($cSiO_2$) with a thickness of 106 ± 4 nm is clearly distinguishable from the two adjacent porous silica layers ($pSiO_2/hSiO_2$); however, the latter two are difficult to differentiate from each other due to their similar electron contrast (Fig. 6 (c, d)). Consequently, only their combined thickness was determined from the cross-sectional SEM images (Table 6), yielding values of 95 ± 8 nm and 109 ± 4 nm for the $Si/TiO_2/pSiO_2/hSiO_2$ and $Si/TiO_2/cSiO_2/pSiO_2/hSiO_2$ structures, respectively.

Comparison of the thicknesses determined by cross-sectional SEM (Table 6) and spectroscopic ellipsometry (Table 4) reveals a reasonable overall agreement between the two techniques. However, the SEM-derived thicknesses are consistently lower than the corresponding SE values for all investigated coatings. This systematic difference suggests that the discrepancy does not arise from random measurement uncertainty but rather reflects the different physical quantities determined by the two techniques.

3.5. Surface roughness analysis by AFM

The surface morphology of the glass-supported single-layer $hSiO_2$ sample and the three- and four-layer $glass/TiO_2/pSiO_2/hSiO_2$ and $glass/TiO_2/cSiO_2/pSiO_2/hSiO_2$ coating systems was further characterized by atomic force microscopy (AFM). Quantitative surface characterization based on the AFM images (Fig. 7) was performed by evaluating the root mean square roughness (Sq) and mean roughness (Sa), as summarized in Table 7. The corresponding Sq and Sa values are in the sub-nanometer range, indicating that all investigated samples show very smooth surfaces with only minor differences in surface roughness. The $glass/hSiO_2$ single-layer reference sample showed Sq and Sa values of 0.274 nm and 0.218 nm, respectively, whereas slightly lower values of 0.194 nm and 0.155 nm were obtained for the $glass/TiO_2/pSiO_2/hSiO_2$ sample.

Table 6
Thickness values of the TiO_2, $cSiO_2$, and combined $pSiO_2/hSiO_2$ coatings determined from the cross-sectional SEM images (Fig. 6 (b, d)). Thickness was measured at thirty points on a single cross-sectional SEM image for each sample.

Sample	TiO_2 d [nm]	$cSiO_2$ d [nm]	combined $pSiO_2/hSiO_2$ d [nm]
$Si/TiO_2/pSiO_2/hSiO_2$	116 ± 3	-	95 ± 8
$Si/TiO_2/cSiO_2/pSiO_2/hSiO_2$	103 ± 4	106 ± 4	109 ± 4

Similarly low roughness values of 0.198 nm and 0.159 nm were obtained for the $glass/TiO_2/cSiO_2/pSiO_2/hSiO_2$ sample. These results are consistent with the homogeneous surface morphology observed by SEM (Fig. 6).

Although the two multilayer systems resulted in slightly lower Sq and Sa values than the single-layer $glass/hSiO_2$ reference, the differences are small in absolute terms. Overall, the AFM results confirm the formation of very smooth surfaces for all investigated coating systems, with only minor differences in their quantitative roughness parameters.

3.6. Wettability of the prepared samples

The surface wettability of the prepared samples was characterized by water contact angle measurements. Three samples of the same coating type were analyzed, with three droplets per sample. Measurements were performed using the sessile drop method and drop build-up technique. The wetting behaviour of the multilayer structures incorporating a hybrid silica ($hSiO_2$) top layer was investigated to assess its contribution to the overall surface functionality. The incorporation of methyl groups ($–CH_3$) into the $hSiO_2$ network contributes to the water-repellent character of the coating by reducing the polarity of the hybrid silica surface [34].

The advancing and receding contact angles along with the calculated contact angle hysteresis and equilibrium contact angles obtained for the samples on glass and silicon substrates are presented in Table 8 and Table 9, respectively.

For samples deposited on glass substrates, the equilibrium water contact angles ranged between 81 ± 2° and 83 ± 1°, indicating moderate wettability rather than strongly hydrophobic behaviour. The contact

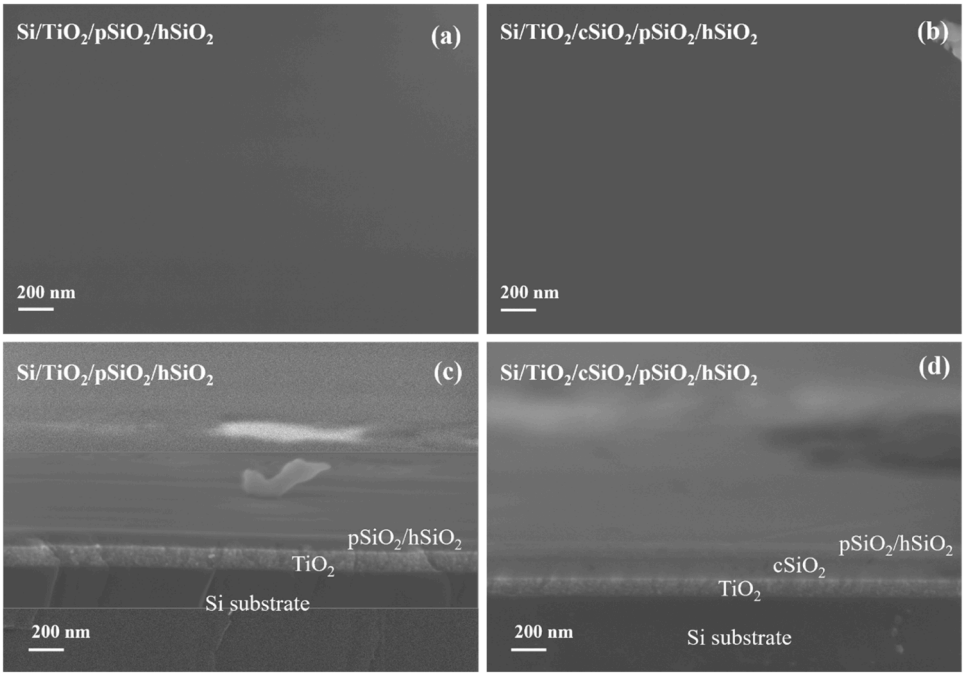


Fig. 6. Representative top-view (a, b) and cross-sectional (c, d) SEM images of the $Si/TiO_2/pSiO_2/hSiO_2$ (a, c) and $Si/TiO_2/cSiO_2/pSiO_2/hSiO_2$ (b, d) samples.

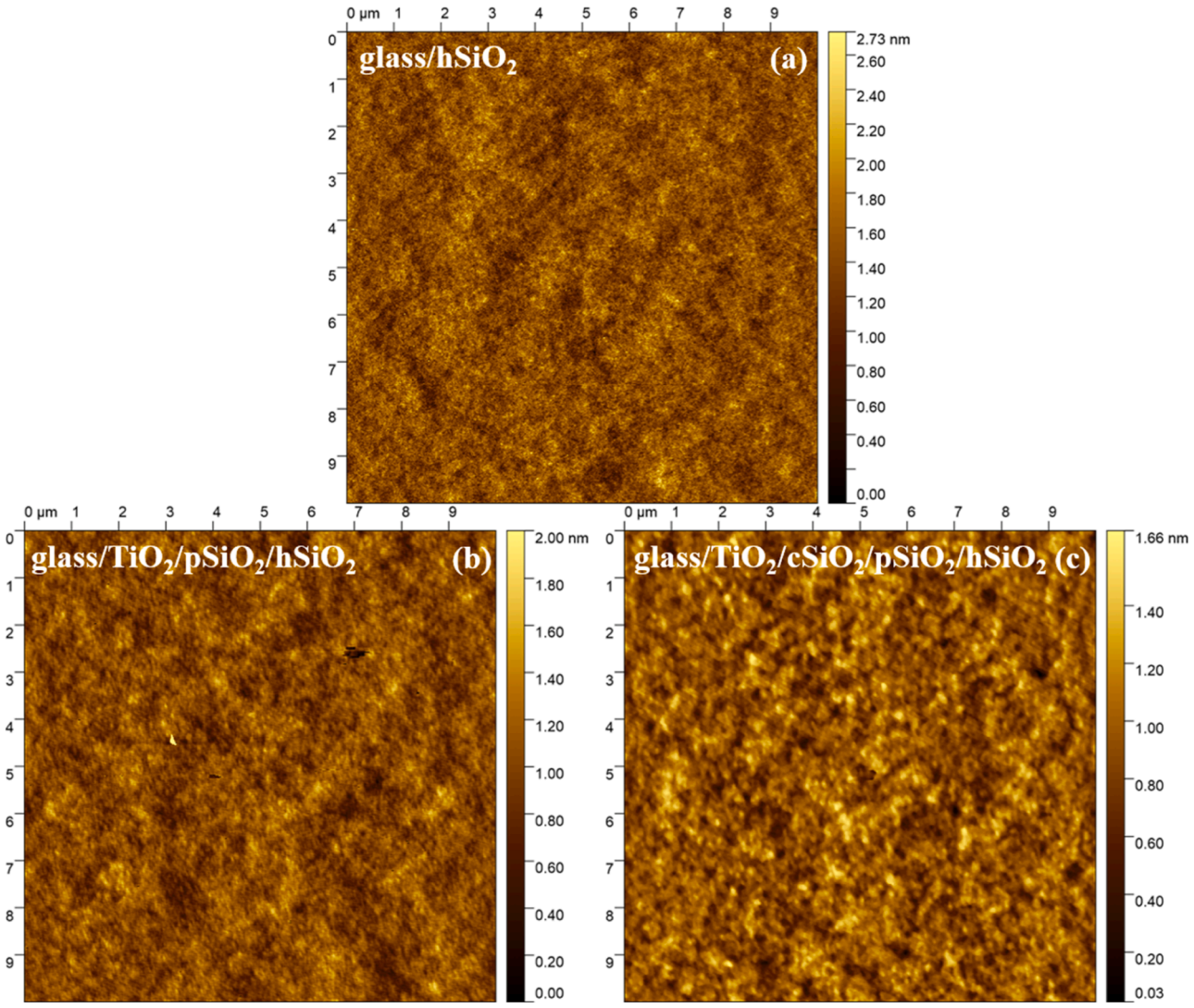


Fig. 7. Top-view AFM images of the glass/$hSiO_2$ (a), glass/TiO_2/$pSiO_2$/$hSiO_2$ (b), and glass/TiO_2/$cSiO_2$/$pSiO_2$/$hSiO_2$ (c) samples.

Table 7
Root mean square (RMS) roughness (Sq) and mean roughness (Sa) values calculated for the glass/$hSiO_2$, glass/TiO_2/$pSiO_2$/$hSiO_2$, and glass/TiO_2/$cSiO_2$/$pSiO_2$/$hSiO_2$ sample surfaces shown in Fig. 7.

Sample	Sq [nm]	Sa [nm]
glass/ $hSiO_2$	0.274	0.218
glass/TiO_2/$pSiO_2$/$hSiO_2$	0.194	0.155
glass/TiO_2/$cSiO_2$/$pSiO_2$/$hSiO_2$	0.198	0.159

Table 8
Advancing (Θ_A) and receding (Θ_R) contact angles measured with ultrapure water on the surface of samples on glass substrates, including calculated contact angle hysteresis (H) and equilibrium contact angle (Θ) values. Three samples of the same coating type were analyzed, with three droplets per sample. Values are reported as mean ± sample standard deviation.

Sample	Θ_A (°)	Θ_R (°)	H (°)	Θ (°)
glass/TiO_2/$pSiO_2$/$hSiO_2$	87 ± 1	78 ± 1	9 ± 1	83 ± 1
glass/TiO_2/$cSiO_2$/$pSiO_2$/$hSiO_2$	84 ± 1	78 ± 2	6 ± 1	81 ± 2

angle hysteresis varied between 6 ± 1° and 9 ± 1°, indicating relatively low droplet pinning and facilitating water droplet mobility on the coating surfaces (Table 8).

Table 9
Advancing (Θ_A) and receding (Θ_R) contact angles measured with ultrapure water on the surface of samples on silicon substrates, including calculated contact angle hysteresis (H) and equilibrium contact angle (Θ) values. Three samples of the same coating type were analyzed, with three droplets per sample. Values are reported as mean ± sample standard deviation.

Sample	Θ_A (°)	Θ_R (°)	H (°)	Θ (°)
Si/TiO_2/$pSiO_2$/$hSiO_2$	68 ± 3	60 ± 4	8 ± 2	64 ± 3
Si/TiO_2/$cSiO_2$/$pSiO_2$/$hSiO_2$	64 ± 2	57 ± 1	7 ± 2	61 ± 2

In the case of coating systems on silicon substrates, equilibrium water contact angles were between 56 ± 4° and 64 ± 3°, with hysteresis values in the range of 7 ± 2° to 9 ± 2°. Thus, the silicon-supported coatings showed higher water wettability than the corresponding glass-supported coatings, while their contact angle hysteresis remained relatively low (Table 9).

Upon exposure to a water jet, water droplets were readily shed from the sample surfaces. However, this effect was less pronounced for the samples prepared on silicon substrates, where a few droplets remained on the surface after the water jet was removed. The observed droplet removal is consistent with the relatively low contact angle hysteresis measured for the coatings, which indicates weak droplet pinning.

The significant difference observed between the water contact angle

values of the multi-layer systems on the two different supports may be related to the influence of the underlying substrate.

3.7. Environmental and mechanical stability of coatings prepared on glass substrates

To quantitatively assess the optical stability of the prepared single- and multi-layer coatings, the root mean square error of the transmittance spectra (RMSE, %) was calculated over the 350–1100 nm spectral range by comparing the transmittance spectra recorded before and after each of the three degradation tests (Table 10).

As shown in Table 10, all samples maintained low RMSE values (< 0.5%) following 6 h of water soaking and dry heat exposure, indicating good optical stability under these conditions. Under mechanical abrasion testing, the RMSE values increased for all samples, reaching a maximum of 1.24% for the glass/TiO_2/$pSiO_2$/$hSiO_2$ sample. Abrasion scratches were also visible on the surfaces of the glass/TiO_2/$pSiO_2$/$hSiO_2$ and glass/TiO_2/$cSiO_2$/$pSiO_2$/$hSiO_2$ samples. However, it should be noted that an RMSE of 1.24% is still relatively low; for comparison, independently prepared samples of the same coating type showed RMSE values of up to 1.76% under similar measurement conditions. The adhesion tape test indicated strong coating adhesion to the substrate, as the tape could not be cleanly and quickly (1 s/25 mm of tape) removed, and adhesive residue remained on the coating surface. Because the adhesive residue would interfere with the optical measurements, transmittance was not evaluated after the adhesion test.

Table 10
Root mean square error (RMSE) values calculated from the transmittance spectra after the dry heat, ultrapure water immersion, and abrasion tests for the glass/$hSiO_2$, glass/TiO_2/$pSiO_2$/$hSiO_2$, and glass/TiO_2/$cSiO_2$/$pSiO_2$/$hSiO_2$ samples.

Sample	RMSE of the transmittance [%]		
	Dry heat at 70 °C	Ultrapure water at 23 ± 2 °C	Abrasion test
glass/$hSiO_2$	0.11	0.30	0.39
glass/TiO_2/$pSiO_2$/$hSiO_2$	0.21	0.37	1.24
glass/TiO_2/$cSiO_2$/$pSiO_2$/$hSiO_2$	0.21	0.45	1.02

4. Conclusions

In this study, titania- and silica-based multilayer sol–gel coatings with spectrally selective light transmission and water-repellent surface functionality were developed on glass substrates using a model-guided experimental approach. The optical modelling provided a starting point for identifying suitable combinations of layer thickness and effective refractive index, while the final three- and four-layer structures were developed and optimized experimentally. The targeted spectral response was selected to meet the requirements of photovoltaic cover-glass applications, particularly for perovskite-based solar cells, where efficient transmission in the visible spectral region is important for light harvesting, while reducing the transmission of near-infrared radiation can help limit non-photocontributing radiation and associated heating.

The developed multilayer systems combined TiO_2 and SiO_2 layers with different thicknesses, effective refractive indices, and porous structures. The individual layers showed distinct structural and optical characteristics resulting from the different sol–gel synthesis routes. These differences, together with the layer thicknesses and their combination within the multilayer systems, contributed to tailoring the overall spectral response toward the targeted optical characteristics.

The optimized glass/TiO_2/$pSiO_2$/$hSiO_2$ and glass/TiO_2/$cSiO_2$/$pSiO_2$/$hSiO_2$ systems increased the average visible transmittance by 2.3 ± 0.4% and 2.3 ± 0.2%, respectively, while reducing the average near-infrared transmittance by 9.4 ± 0.6% and 7.8 ± 0.2%. Maximum transmittance values of 99.17 ± 0.11% at 498 ± 4 nm and 99.62 ± 0.07% at 554 ± 5 nm were obtained for the two systems, respectively. The $hSiO_2$-free structures showed negative average transmittance change values in the visible range, indicating that the hybrid silica top layer contributed to the enhancement of visible-light transmittance. Thus, the multilayer coatings provided a combination of enhanced transmission in the visible region and reduced near-infrared transmission relevant to spectrally selective photovoltaic cover-glass applications.

The surface characteristics of the coatings were also closely related to their functionality. Atomic force microscopy measurements showed sub-nanometer surface roughness, root mean square roughness (Sq) values of 0.194–0.198 nm and mean roughness (Sa) values of 0.155–0.159 nm for the two optimized multilayer systems, indicating very smooth surfaces. The hybrid silica top layer, containing methyl groups, provided water-repellent surface functionality, characterized by low contact angle hysteresis and efficient droplet removal under a water jet. Equilibrium water contact angles of 81–83° and hysteresis values of 6–9° were obtained, indicating moderate wettability combined with low droplet pinning rather than strongly hydrophobic behaviour.

The coatings also showed good optical stability after dry-heat exposure and ultrapure water immersion, with root mean square error (RMSE) values below 0.5%, whereas abrasion resulted in visible surface scratches and a moderate increase in the RMSE values. The adhesion test indicated strong adhesion of the coatings to the substrate. Overall, the results demonstrate that combining controlled layer thickness, effective refractive index, porous structure, and surface properties through sol–gel processing enables the development of multifunctional oxide coating systems with tailored optical and wetting characteristics. The demonstrated combination of spectral selectivity, smooth surface morphology, water-repellent functionality, and optical stability makes these multilayer coatings promising candidates for functional photovoltaic cover-glass surfaces.

CRediT authorship contribution statement

Kinga Kovács: Writing – original draft, Investigation, Formal analysis, Data curation. **János Madarász:** Investigation. **Norbert Nagy:** Formal analysis, Investigation. **Dániel Zámbó:** Investigation. **Zoltán Hórvölgyi:** Writing – review & editing, Conceptualization. **Emőke Albert:** Writing – review & editing, Supervision, Investigation, Conceptualization.

Declaration of competing interest

The authors declare that they have no known competing financial interests or personal relationships that could have appeared to influence the work reported in this paper.

Acknowledgements

The authors gratefully acknowledge Levente Kovács for his assistance in implementing the computational framework for the thin-film models.

E.A. acknowledges the financial support of the “Parents Back to Science” grant from the Budapest University of Technology and Economics.

The authors acknowledge Semilab Semiconductor Physics Laboratory Co. Ltd. for providing the opportunity to perform the spectroscopic ellipsometry and ellipsometric porosimetry measurements.

Data availability

Data will be made available on request.

References

[1] I.L. Repins, D.C. Jordan, M. Woodhouse, M. Theristis, J.S. Stein, H.P. Seigneur, D. J. Colvin, J.F. Karas, A.N. McPherson, C. Deline, Long-term impact of light- and elevated temperature-induced degradation on photovoltaic arrays, MRS Bull. 48 (6) (2023) 589–601, https://doi.org/10.1557/s43577-022-00438-8.

[2] J. Karas, I. Repins, K.A. Berger, B. Kubicek, F. Jiang, D. Zhang, J. Jaubert, A. B. Cueli, T. Sample, B. Jaeckel, M. Pander, E. Fokuhl, M.B. Koentopp, F. Kersten, J. Choi, B. Bora, C. Banerjee, S. Wendlandt, T. Erion-Lorico, K.J. Sauer, J. Tsan, M. Pravettoni, M. Caccivio, G. Bellenda, C. Monokroussos, H. Maaroufi, Results from an international interlaboratory study on light- and elevated temperature-induced degradation in solar modules, Prog. Photovolt. Res. Appl. 30 (11) (2022) 1255–1269, https://doi.org/10.1002/pip.3573.

[3] M. Theristis, J.S. Stein, C. Deline, D. Jordan, C. Robinson, W. Sekulic, A. Anderberg, D.J. Colvin, J. Walters, H. Seigneur, B.H. King, Onymous early-life performance degradation analysis of recent photovoltaic module technologies, Prog. Photovolt. Res. Appl. 31 (2) (2023) 149–160, https://doi.org/10.1002/pip.3615.

[4] L. Ye, Y. Zhang, X. Zhang, T. Hu, R. Ji, B. Ding, B. Jiang, Sol–Gel preparation of SiO_2/TiO_2/SiO_2–TiO_2 broadband antireflective coating for solar cell cover glass, Sol. Energy Mater. Sol. Cells 111 (2013) 160–164, https://doi.org/10.1016/j.solmat.2012.12.037.

[5] X. Shen, S. Jiang, X. Wang, H. Zhou, Z. Yu, Suppressing optical losses in solar cells via multifunctional and large-scale geometric arrays, Nanomaterials 13 (20) (2023) 2766, https://doi.org/10.3390/nano13202766.

[6] K. Hasan, S.B. Yousuf, M.S.H.K. Tushar, B.K. Das, P. Das, M.S. Islam, Effects of different environmental and operational factors on the PV performance: a comprehensive review, Energy Sci. Eng. 10 (2) (2022) 656–675, https://doi.org/10.1002/ese3.1043.

[7] M. Jošt, B. Lipovšek, B. Glažar, A. Al-Ashouri, K. Brecl, G. Matič, A. Magomedov, V. Getautis, M. Topič, S. Albrecht, Perovskite solar cells go outdoors: field testing and temperature effects on energy yield, Adv. Energy Mater 10 (25) (2020) 2000454, https://doi.org/10.1002/aenm.202000454.

[8] J. Zhi, L.-Z. Zhang, Durable superhydrophobic surface with highly antireflective and self-cleaning properties for the glass covers of solar cells, Appl. Surf. Sci. 454 (2018) 239–248, https://doi.org/10.1016/j.apsusc.2018.05.139.

[9] L. Xu, Z. Geng, J. He, G. Zhou, Mechanically robust, thermally stable, broadband antireflective, and superhydrophobic thin films on glass substrates, ACS Appl. Mater. Interfaces 6 (12) (2014) 9029–9035, https://doi.org/10.1021/am5016777.

[10] H. Sayed, Z.S. Matar, M. Al-Dossari, A.F. Amin, N.S.A. El-Gawaad, A.H. Aly, The design and optimization of an anti-reflection coating and an intermediate reflective layer to enhance tandem solar cell photons capture, Crystals 12 (1) (2021) 57, https://doi.org/10.3390/cryst12010057.

[11] A.M. Oni, A.S.M. Mohsin, M.M. Rahman, M.B. Hossain Bhuian, A comprehensive evaluation of solar cell technologies, associated loss mechanisms, and efficiency enhancement strategies for photovoltaic cells, Energy Rep. 11 (2024) 3345–3366, https://doi.org/10.1016/j.egyr.2024.03.007.

[12] W.L. Leong, Z. Ooi, D. Sabba, C. Yi, S.M. Zakeeruddin, M. Graetzel, J.M. Gordon, E. A. Katz, N. Mathews, Identifying fundamental limitations in halide perovskite solar cells, Adv. Mater. 28 (12) (2016) 2439–2445, https://doi.org/10.1002/adma.201505480.

[13] E. Aydin, T.G. Allen, M. De Bastiani, L. Xu, J. Ávila, M. Salvador, E. Van Kerschaver, S. De Wolf, Interplay between temperature and bandgap energies on the outdoor performance of perovskite/silicon tandem solar cells, Nat. Energy 5 (11) (2020) 851–859, https://doi.org/10.1038/s41560-020-00687-4.

[14] T. Moot, J.B. Patel, G. McAndrews, E.J. Wolf, D. Morales, I.E. Gould, B.A. Rosales, C.C. Boyd, L.M. Wheeler, P.A. Parilla, S.W. Johnston, L.T. Schelhas, M.D. McGehee, J.M. Luther, Temperature coefficients of perovskite photovoltaics for energy yield calculations, ACS Energy Lett. 6 (5) (2021) 2038–2047, https://doi.org/10.1021/acsenergylett.1c00748.

[15] S.S. Dipta, A. Uddin, G. Conibeer, Enhanced light management and optimization of Perovskite solar cells incorporating wavelength dependent reflectance modeling, Heliyon 8 (11) (2022) e11380, https://doi.org/10.1016/j.heliyon.2022.e11380.

[16] O. Dupré, R. Vaillon, M.A. Green, A full thermal model for photovoltaic devices, Sol. Energy 140 (2016) 73–82, https://doi.org/10.1016/j.solener.2016.10.033.

[17] B. Chen, D. Yao, P. Dong, J. He, J. Su, B. Ma, F. Chen, N. Tian, G. Zheng, M. Chen, J. Wang, Y. Peng, Q. Han, Y. Gao, F. Long, UV-resistant nanostructured anti-reflective film for achieving efficiency enhancement of perovskite solar cells and potential of fabricating large-scale Cu(In, Ga)Se_2 solar cells, ACS Appl. Mater. Interfaces 17 (6) (2025) 9266–9277, https://doi.org/10.1021/acsami.4c18588.

[18] J. Wei, Q. Wang, J. Huo, F. Gao, Z. Gan, Q. Zhao, H. Li, Mechanisms and suppression of photoinduced degradation in perovskite solar cells, Adv. Energy Mater. 11 (3) (2021) 2002326, https://doi.org/10.1002/aenm.202002326.

[19] C. Fei, A. Kuvayskaya, X. Shi, M. Wang, Z. Shi, H. Jiao, T.J. Silverman, M. Owen-Bellini, Y. Dong, Y. Xian, R. Scheidt, X. Wang, G. Yang, H. Gu, N. Li, C.J. Dolan, Z.J. D. Deng, D.N. Cakan, D.P. Fenning, Y. Yan, M.C. Beard, L.T. Schelhas, A. Sellinger, J. Huang, Strong-bonding hole-transport layers reduce ultraviolet degradation of perovskite solar cells, Science 384 (6700) (2024) 1126–1134, https://doi.org/10.1126/science.adi4531.

[20] T. Chen, J. Xie, P. Gao, Ultraviolet photocatalytic degradation of perovskite solar cells: progress, challenges, and strategies, Adv. Energy Sustain. Res. 3 (6) (2022) 2100218, https://doi.org/10.1002/aesr.202100218.

[21] J. Werner, J. Geissbühler, A. Dabirian, S. Nicolay, M. Morales-Masis, S.D. Wolf, B. Niesen, C. Ballif, Parasitic absorption reduction in metal oxide-based transparent electrodes: application in perovskite solar cells, ACS Appl. Mater. Interfaces 8 (27) (2016) 17260–17267, https://doi.org/10.1021/acsami.6b04425.

[22] A. Fell, J. Greulich, F. Feldmann, C. Messmer, J. Schön, M. Bivour, M.C. Schubert, S.W. Glunz, Modeling parasitic absorption in silicon solar cells with a near-surface absorption parameter, Sol. Energy Mater. Sol. Cells 236 (2022) 111534, https://doi.org/10.1016/j.solmat.2021.111534.

[23] B.M. Cote, I.M. Slauch, M.G. Deceglie, T.J. Silverman, V.E. Ferry, Light management in bifacial photovoltaics with spectrally selective mirrors, ACS Appl. Energy Mater. 4 (6) (2021) 5397–5402, https://doi.org/10.1021/acsaem.1c01236.

[24] O. Dupré, R. Vaillon, M.A. Green, Thermal issues in photovoltaics and existing solutions. Thermal Behavior of Photovoltaic Devices, Springer International Publishing, Cham, 2017, pp. 1–28, https://doi.org/10.1007/978-3-319-49457-9_1.

[25] M. Peters, J.C. Goldschmidt, P. Löper, B. Groß, J. Üpping, F. Dimroth, R. B. Wehrspohn, B. Bläsi, Spectrally-selective photonic structures for PV applications, Energies 3 (2) (2010) 171–193, https://doi.org/10.3390/en3020171.

[26] T. Yasuda, A. Kinoshita, Sol–gel multilayer coatings for spectral control of thermal radiation, J. Ceram. Soc. Jpn. 132 (9) (2024) 555–559, https://doi.org/10.2109/jcersj2.24043.

[27] K. Tonooka, N. Kikuchi, Super-hydrophilic and solar-heat-reflective coatings for smart windows, Thin Solid Films 532 (2013) 147–150, https://doi.org/10.1016/j.tsf.2012.11.148.

[28] C.J. Brinker, G.C. Frye, A.J. Hurd, C.S. Ashley, Fundamentals of sol-gel dip coating, Thin Solid Films 201 (1) (1991) 97–108, https://doi.org/10.1016/0040-6090(91)90158-T.

[29] P. Dulian, J. Jaglarz, Spectroscopic ellipsometry and optical modeling of sol-gel-derived oxide thin films. *Thin Films - Synthesis and Characterization [Working Title]*, IntechOpen, 2026, https://doi.org/10.5772/intechopen.1016061.

[30] M. Syed, J. Mvula, B. Anderson, B. Cook, E. Hollins, P. Taylor, I.S. Syed, Sol–gel spin-coated multilayer nc-Si thin films on silicon substrates: controlled growth, composition, and electronic structure, J. Mater. Sci. Res. 15 (1) (2026) 27, https://doi.org/10.5539/jmsr.v15n1p27.

[31] H.B. Wafula, R.J. Musembi, A.O. Juma, P. Tonui, J. Simiyu, T. Sakwa, D. Prakash, K.D. Verma, Compositional analysis and optical properties of Co doped TiO_2 thin films fabricated by spray pyrolysis method for dielectric and p hotocalytic applications, Optik (Stuttg) 128 (2017) 212–217, https://doi.org/10.1016/j.ijleo.2016.08.107.

[32] H. Wafula, A. Juma, T. Sakwa, R. Musembi, J. Simiyu, A surface photovoltage study of surface defects on Co-doped TiO_2 thin films deposited by spray pyrolysis, Coatings 6 (3) (2016) 30, https://doi.org/10.3390/coatings6030030.

[33] E. Albert, N. Cotolan, N. Nagy, G. Sáfrán, G. Szabó, L.-M. Mureşan, Z. Hórvölgyi, Mesoporous silica coatings with improved corrosion protection properties, Microporous Mesoporous Mater. 206 (2015) 102–113, https://doi.org/10.1016/j.micromeso.2014.12.021.

[34] A. Ábrahám, L. Kócs, E. Albert, B. Tegze, B. Szolnoki, N. Nagy, G. Sáfrán, P. Basa, Z. Hórvölgyi, Durability of microporous hybrid silica coatings: optical and wetting properties, Thin Solid Films 699 (2020) 137914, https://doi.org/10.1016/j.tsf.2020.137914.

[35] G. Szabó, E. Albert, J. Both, L. Kócs, G. Sáfrán, A. Szöke, Z. Hórvölgyi, L. M. Mureşan, Influence of embedded inhibitors on the corrosion resistance of zinc coated with mesoporous silica layers, Surf. Interfaces 15 (2019) 216–223, https://doi.org/10.1016/j.surfin.2019.03.007.

[36] E. Hild, A. Deák, L. Naszályi, Ö. Sepsi, N. Ábrahám, Z. Hórvölgyi, Use of the optical admittance function and its WKB approximation to simulate and evaluate transmittance spectra of graded-index colloidal films, J. Opt. Pure Appl. Opt. 9 (10) (2007) 920–930, https://doi.org/10.1088/1464-4258/9/10/023.

[37] E. Albert, P. Basa, B. Fodor, Z. Keresztes, J. Madarász, P. Márton, D. Olasz, A. S. Rácz, G. Sáfrán, T. Szabó, B. Tegze, T. Höltzl, Z. Hórvölgyi, Experimental and computational synthesis of TiO_2 sol–Gel coatings, Langmuir 41 (1) (2025) 704–718, https://doi.org/10.1021/acs.langmuir.4c03959.

[38] E. Nichelatti, M. Montecchi, R.M. Montereali, Optical reflectance and transmittance of a multilayer coating affected by refractive-index inhomogeneity, interface roughness, and thickness wedge, J. Non-Cryst. Solids 355 (18–21) (2009) 1115–1118, https://doi.org/10.1016/j.jnoncrysol.2008.11.040.

[39] H.A. MacLeod, *Thin-Film Optical Filters*; Series in Optics and Optoelectronics, CRC Press, 2010.

[40] C. Trapalis, N. Todorova, M. Anastasescu, C. Anastasescu, M. Stoica, M. Gartner, M. Zaharescu, T. Stoica, Atomic force microscopy study of TiO_2 sol–Gel films thermally treated under NH_3 atmosphere, Thin Solid Films 517 (23) (2009) 6243–6247, https://doi.org/10.1016/j.tsf.2009.02.070.

[41] E. Albert, P.A. Albouy, A. Ayral, P. Basa, G. Csík, N. Nagy, S. Roualdès, V. Rouessac, G. Sáfrán, Á. Suhajda, Z. Zolnai, Z. Hórvölgyi, Antibacterial properties of Ag–TiO_2 composite sol–Gel coatings, RSC Adv. 5 (73) (2015) 59070–59081, https://doi.org/10.1039/C5RA05990A.

[42] M. Klotz, A. Ayral, C. Guizard, L. Cot, Synthesis conditions for hexagonal mesoporous silica layers, J. Mater. Chem. 10 (3) (2000) 663–669, https://doi.org/10.1039/a906181i.

[43] T.S. Vaishnavi, P. Haridoss, C. Vijayan, Optical properties of zinc oxide nanocrystals embedded in mesoporous silica, Mater. Lett. 62 (10–11) (2008) 1649–1651, https://doi.org/10.1016/j.matlet.2007.09.051.

[44] M. Matheron, A. Bourgeois, A. Brunet-Bruneau, P.-A. Albouy, J. Biteau, T. Gacoin, J.-P. Boilot, Highly ordered CTAB-templated organosilicate films, J. Mater. Chem. 15 (44) (2005) 4741, https://doi.org/10.1039/b510554d.

[45] S.W. Boettcher, J. Fan, C.-K. Tsung, Q. Shi, G.D. Stucky, Harnessing the sol–Gel process for the assembly of non-silicate mesostructured oxide materials, Acc. Chem. Res. 40 (9) (2007) 784–792, https://doi.org/10.1021/ar6000389.

[46] Https://Refractiveindex.Info/?shelf=main&book=SiO2&page=Rodriguez-de_Marcos.

[47] Http://Gwyddion.Net.

[48] E. Wolfram, R. Faust, in: J.F. Padday (Ed.), Wetting, Spreading and Adhesion, Academic Press, New York, 1978.
[49] International Organization for Standardization ISO, ISO 9022-2:2015: Optics and Photonics Environmental Test Methods Part 2: Cold, Heat and Humidity, ISO, Geneva, Switzerland, 2015.
[50] International Organization for Standardization, ISO 9211-4: 2012: Optics and Photonics Optical Coatings Part 4: Specific Test Methods, ISO, Geneva, Switzerland, 2012.
[51] H.E. Swanson, H.F. McMurdie, M.C. Morris, E.H. Evans, Evans, Standard X-Ray Diffraction Powder Patterns, National Bureau of Standards Monograph 25, Section 7, U.S, Government Printing Office, Washington, D.C., 1969.